Simultaneous Multiband Demodulation Using a Rydberg Atomic Sensor

David H. Meyer ●,[*] Joshua C. Hill ●, Paul D. Kunz ●, and Kevin C. Cox ●

DEVCOM Army Research Laboratory, Adelphi, Maryland 20783, USA

Electric field sensors based on Rydberg atoms offer unique capabilities, relative to traditional sensors, for detecting radio-frequency (rf) signals. In this work, we demonstrate simultaneous demodulation and detection of five rf tones spanning nearly two decades (six octaves), from 1.7 GHz to 116 GHz. We show continuous recovery of the phase and amplitude of each tone and report on the sensitivity of the system and its bandwidth capabilities for multiband detection. We use these capabilities to demonstrate a digital communication protocol, simultaneously receiving on-off-keyed binary data from four bands spanning nearly one decade of frequency.

I. INTRODUCTION

The radio-frequency (rf) spectrum is typically defined as electromagnetic waves with frequencies between 30 kHz and 300 GHz, a range of six decades. Humans use this entire range for applications such as communication, remote sensing, navigation, and timekeeping. There is increasing interest in rf sensors based on Rydberg states of atoms, with a highly excited electron, because they exhibit sensitivity and resonances across the entire range [1–3].

In contrast, traditional rf sensors based on resonant antennas typically have limited bandwidth, operating over a fraction of a decade. The use of multiple rf bands usually requires more than one antenna, increasing the size and complexity of a system. Further, the use of multiple antennas often leads to colocation interference, where each antenna interferes with the performance of its neighbor. Rydberg atoms offer a unique path to overcome these technological challenges.

Recent work in the field of Rydberg sensing has pointed to the capability of Rydberg atoms to detect rf fields across the entire spectrum, using various methods including multiple atomic species [4], Stark tuning of resonances [5], utilization of the off-resonant Stark effect [6–8], multiphoton resonances [9], and operation across the vast forest of Rydberg resonances [10], with demonstrations ranging from the terahertz [11] to the quasi-dc [7,12] regimes. We extend upon this work by demonstrating simultaneous multiband demodulation using multiple Rydberg states.

First, we introduce how the square-law sensitivity of Rydberg atoms in the off-resonant regime allows simultaneous demodulation. Second, we introduce the experimental apparatus and demonstrate demodulation and detection of five tones, ranging from 1.7 GHz to 116 GHz. We show

that the amplitude and phase of each tone can be recovered simultaneously, by demodulating into different portions of the base band, with approximately 6 MHz of instantaneous bandwidth. Finally, we demonstrate simultaneous detection of binary digital signals with four tones at bit rates of up to 40 kbit/s with bit-error rates better than 0.6 kbit/s.

II. THEORY BACKGROUND

The level diagram of the Rydberg sensor is shown in Fig. 1(a). We operate the sensor by performing spectroscopy on a single Rydberg "target" state. Interaction with multiple rf tones (denoted by the colored arrows) leads to simultaneous perturbations in the state energy. These perturbations are measured spectroscopically via a ladder–electromagnetically induced transparency (EIT) scheme comprised of a probe and a coupling laser.

In order to simultaneously detect the perturbations on the target state from multiple rf signals, it is important that the signal perturbations combine linearly in the spectroscopic response, allowing for a linear recovery of each signal tone. This condition can be stated as

$$d\omega = \sum_i d\omega_i,\qquad(1)$$

where $d\omega$ is the total frequency shift of the target Rydberg state and $d\omega_i$ is the frequency shift due to a single rf field E_i. If this condition is not satisfied, the spectroscopic response to multiple rf fields is nonlinear, where simultaneous signal recovery generally becomes complex and interdependent. In this work, we employ rf couplings to the target state that satisfy Eq. (1).

Our sensor simultaneously detects five signals, with frequencies 1.72, 12.11, 27.42, 65.11, and 115.75 GHz. The highest four of these signals operate somewhat detuned
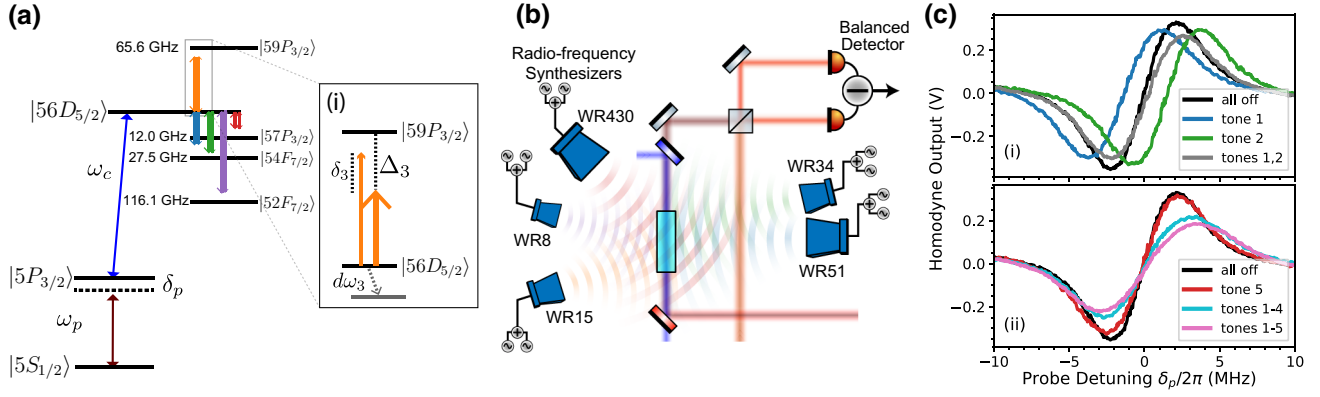
_____
[*]david.h.meyer3.civ@army.mil

FIG. 1. The energy diagrams and the experimental configuration. (a) The energy-level diagram of the full system. Optical spectroscopy is done in a ladder-EIT configuration (denoted by the maroon and blue arrows). The microwave couplings are shown as arrows branching from the $56D_{5/2}$ state. The resonant frequencies of the transitions to nearby Rydberg states are shown. The inset (i) shows the energy-level diagram for off-resonant heterodyne measurements using Rydberg states. A strong local oscillator (LO) field, detuned from atomic resonance, produces a large Stark shift $d\omega_i$ of the target Rydberg state. A weak signal tone, detuned from the LO field, produces beats in the Stark shift of the target state that can be measured spectroscopically. (b) A simplified diagram of the experimental apparatus. The horns corresponding to tones 1–5 are fed by waveguides of size WR51, WR34, WR15, WR8, and WR430, respectively. (c)(i) Example spectroscopy of the target Rydberg state with and without applied rf with near-detuned couplings. The black trace is the unshifted peak. The blue and green traces correspond to LO 1 or 2 being on, respectively. The gray trace shows both LOs on. (c)(ii) The effect of far-detuned couplings. The red trace shows the observed Stark shifts from LO 5. The cyan trace shows the resulting peak with LOs 1–4 on. The magenta trace shows LOs 1–5 on.

from nearby Rydberg transitions, while the lowest frequency of 1.72 GHz, is far red detuned from all relevant transitions. In this off-resonant regime, the Rydberg energy shifts scale quadratically with the field amplitude

$$d\omega_i = \langle a_i(E_i)^2 \rangle, \qquad (2)$$

where a_i is the polarizability and the angle brackets denote a time average representing the finite instantaneous response bandwidth of the atomic sensor. Working in this detuned regime, in contrast to multiple resonant rf couplings, allows for linear addition of the $d\omega_i$ shifts (for further details, see Appendix A).

In each band, we apply two fields to implement an rf heterodyne measurement, one signal electric field S_i and one local oscillator (LO) $E_i \gg S_i$, as has been demonstrated using resonant rf couplings [13,14]. When the signal and LO fields are far detuned from resonance, the resulting state shift is [8]

$$d\omega_i = a_i \left[\frac{E_i^2}{2} + \frac{S_i^2}{2} + E_i S_i \cos\left(\delta_i t\right) \right]. \qquad (3)$$

The first two terms represent static shifts due to the rms amplitudes of the LO and signal fields. The final term in Eq. (3) represents the signal field demodulated into the sensor base band, with base-band frequency δ_i [15]. Due to the square-law response to the applied field when working off resonance, this term also has heterodyne gain from the amplitude of the LO field itself.

EIT spectroscopy is used to detect the shifted resonance frequency of the target state $d\omega$, which contains information from all of the applied fields $E_i + S_i$ according to Eqs. (1) and (3).

III. EXPERIMENTAL SETUP

The experimental layout and atomic level diagrams are shown in Fig. 1(a). Using two lasers [denoted as "probe" (dark red) and "coupling" (blue)], we perform EIT spectroscopy on the $|56D_{5/2}\rangle$ target state to simultaneously detect five rf signal tones, colored orange, blue, green, purple, and red. The Rydberg demodulation scheme for a single tone is shown in the inset [Fig. 1(a)(i)]. For each tone i, a strong LO field E_i is applied from a microwave horn, with detuning from the target state Δ_i. The corresponding signal field S_i has a small detuning δ_i from the LO and is broadcast from the same corresponding horn to superimpose it with E_i at the atomic sample. By Eq. (3), this leads to a detected base-band signal (a heterodyne beat) with frequency δ_i.

Figure 1(b) depicts the experimental setup. Five separate rf horns are aimed at the Rb vapor cell from approximately 30 cm away. The cell is 7.5 cm long and contains natural-abundance Rb. A narrow transmission resonance (EIT) is observed when the probe laser detuning δ_p is swept across the $|5S_{1/2}\rangle \rightarrow |56D_{5/2}\rangle$ two-photon resonance. These spectroscopy signals are detected using the balanced optical-homodyne configuration described in Ref. [10], operated in the phase quadrature, yielding a

TABLE I.   The rf tone experimental parameters, including the tone number, the nearby Rydberg state being coupled to, the resonance frequency of that coupling ω_0^i, the detuning of the LO field relative to that resonance Δ_i, the typical signal detuning from the LO field δ_i unless otherwise noted, and the signal and LO-field amplitudes at the atomic sample E_i and S_i, as described in Appendix C.

Tone i	State $n\mathrm{L}_J$	ω_0^i (GHz)	Δ_i (GHz)	δ_i (kHz)	E_i (V/m)	S_i (V/m)
1	$57P_{3/2}$	12.01	$+0.1$	75	1.2(1)	0.12(1)
2	$54F_{7/2}$	27.52	-0.1	130	2.4(2)	0.14(1)
3	$59P_{3/2}$	65.61	-0.5	180	17.9(26)	1.5(3)
4	$52F_{7/2}$	116.05	-0.3	240	36.0(36)	1.4(2)
5	$57P_{3/2}$	12.01	-10.287	280	16.0(4)	2.3(1)

dispersive-shaped EIT feature as the probe laser detuning is swept. To avoid ambiguity with the rf signals, we refer to the output homodyne signal as the "output" for the remainder of this paper. For all data shown, except Fig. 1(c), the probe is locked to the center of the EIT dispersive feature, where the slope (and therefore the sensitivity) is largest.

The frequencies of the five rf tones, their index labels, and their respective field amplitudes at the atomic sample are shown in Table I. Tones 1–4 are nearly resonant to a dipole-allowed Rydberg transition between the target state and the nearby state indicated in the table. Tone 5 is far red detuned (> 10 GHz) from all relevant Rydberg transitions. The inclusion of tone 5 in this demonstration highlights the broad operational range of the protocol relative to Rydberg transitions and that multiple tones can interact with the same Rydberg transition. The magnitudes of the signal fields are chosen such that the beat of each tone has approximately the same signal-to-noise ratio; differences in set point primarily reflect differences in the Rydberg sensitivity at that frequency via changes to the atomic polarizability a_i. This sensitivity and the linear dynamic range depend on the specific sensor configuration, including detuning from Rydberg resonances and rf LO powers and frequencies.

The LO and signal fields for tones 1, 2, and 5 are generated directly from commercial signal generators. The LO and signal fields for tones 3 and 4 are produced using synthesizers that are then multiplied by a factor of 6 before being broadcast onto the atoms. Further details of the setup are given in Appendix B.

In Fig. 1(c), we show representative phase-quadrature optical EIT output with various combinations of LO fields applied to the atoms. In Fig. 1(c)(i), we show example probe-sweep-spectroscopy traces for LOs 1 and 2, which are relatively close detuned from Rydberg resonances. The black trace shows the unshifted dispersive resonance. The blue and green traces correspond to LO 1 or 2 being on, respectively, resulting in Stark shifts of the resonance in opposing directions. The gray trace shows both LOs on,

resulting in nominal canceling of the Stark shifts, though the resonance is broadened. This broadening is predominantly the result of populating multiple m_J sublevels of the target state, where each sublevel results in a different dipole moment for the rf field. This specific source of broadening could be mitigated by only populating a single sublevel of the target state. Other potential sources of broadening, such as power broadening or inhomogeneous fields, would manifest similarly and should also be considered when optimizing the sensor performance.

In Fig. 1(c)(ii), we show the effect of far-detuned couplings. The red trace shows the observed Stark shift from LO 5. Due to the large detuning, there is no common shift in one direction, as the sublevels of the $D_{5/2}$ state do not all shift in the same direction (for further details, see Appendix C). The cyan trace shows the dispersive resonance with LOs 1–4 on, resulting in a largely canceled shift but a broader feature. The magenta trace shows LOs 1–5 on, which leads to even more broadening of the dispersive feature. Since the sensitivity of the sensor is related to the slope of this dispersive feature (which converts Stark shifts to spectroscopic changes in the measured homodyne probe phase), broadening from increasing numbers of LO tones limits the number of signals that can be simultaneously measured with a given sensitivity.

IV. RESULTS

A. Simultaneous-tone measurement

We first present data showing simultaneous demodulation of five tones into the base band. We broadcast tones 1–5 onto the atoms and record a time series of the homodyne output for 1 s. The raw output is displayed at the top of Fig. 2(a) and the processed data reveal the tones received from all five bands. The experimental settings are summarized in Table I. In these data, tones 1, 2, and 5 have 0.8-rad sinusoidal phase modulations applied with rates of 205 Hz, 110 Hz, and 100 Hz, respectively. All five tones are distinctly visible in the corresponding power spectrum [Fig. 2(b)(i)], found by taking the Fourier transform of the time trace in Fig. 2(a). An enlarged subset of the power spectrum showing the detailed response in the vicinity of tone 5 is shown in Fig. 2(b)(ii), where the phase-modulation sidebands are evident. We identify the other beats in the spectrum as harmonics and sum-or-difference frequencies of the five fundamental beats. The spurious tones are reduced by more than 20 dB from the fundamental tones and are indicative of a weakly nonlinear process, which we attribute to residual nonlinearity in the optical-homodyne detection. Higher-order effects in the atomic system not considered in this work may also be contributing. We independently identify three spurious tones due to electronic pick-up at 174, 180, and 209 kHz.

We simultaneously recover the phase and amplitude of each individual tone via suitable postprocessing of the
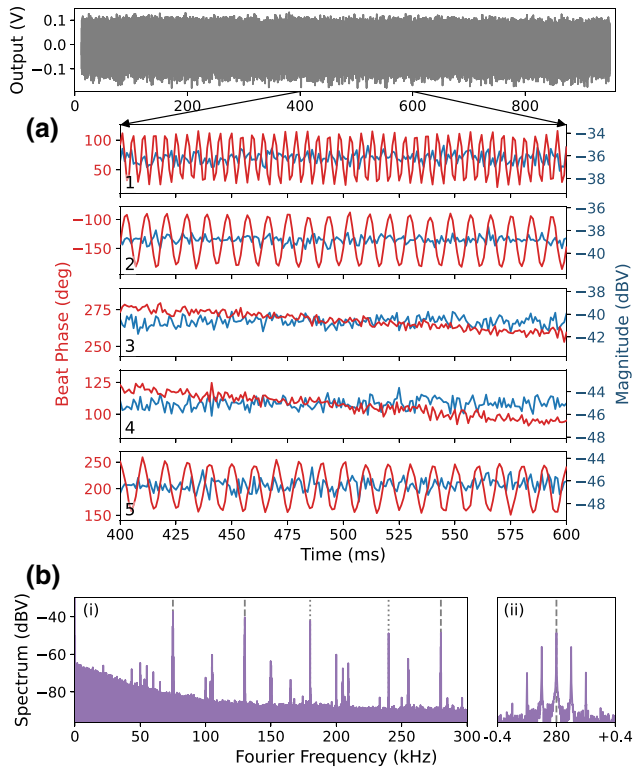
FIG. 2. The simultaneous amplitude and phase recovery of tones spanning over 114 GHz. (a) A single time trace of the photodetector output acquired at 2 MS/s over 1 s. (a) The numbers 1–5 correspond to the amplitude (blue) and phase (red) recovery for tones 1-5, respectively. Tones 1, 2, and 5 have slow phase modulations applied to the signal field of 205 Hz, 110 Hz, and 100 Hz, respectively. (b) The fast Fourier transform (FFT) (i) of the full time trace in (a): the resolution of the FFT is 1 Hz. The inset (ii) presents an enlarged view of the FFT around tone 5 at 280 kHz, showing the clearly resolved phase-modulation sidebands.
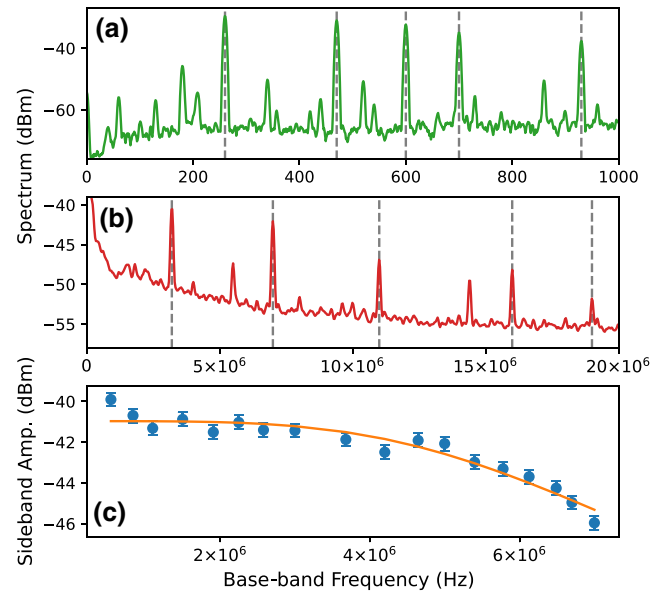

FIG. 3. Spectrum-analyzer measurements of the EIT output with five rf heterodynes applied. The vertical gray dashed lines denote the frequency of the applied beat tones. Each spectrum is an average of 20 traces. (a) Beats at 260, 470, 600, 700, and 930 Hz for tones 1–5: the resolution bandwidth is 4.89 Hz. Note that the $1/f$ noise present in other spectra is suppressed in this frequency range due to active optical-homodyne path stabilization. (b) Beats at 16, 19, 11, 7, and 3.2 MHz for tones 1–5, respectively. While the atomic response reduces beat sizes at higher frequencies, they are still visible. The photodetector frequency response is removed from this data set and the resolution bandwidth is 97.75 kHz. (c) The output beat amplitude versus the modulation frequency. Phase modulation of 0.8 rad is applied to tone 2 (beat frequency at 130 kHz) at varying modulation frequencies. The orange line is a fit to a second-order low-pass function with a 3-dB corner at 6.11(16) MHz. The photodetector response is removed from the data (see Appendix D).

time trace. We take the Fourier transform of the raw data and extract each tone in frequency space with a 1-kHz bandwidth. The amplitude and phase correspond to the magnitude and angle of the complex Fourier component. The phase and amplitude of each beat tone is displayed in Fig. 2(a)(1–5), shown as the red and blue traces, respectively. The amplitudes of each tone are constant, with fluctuations in the recovered amplitude consistent with the Rydberg-sensor noise floor observed in Fig. 2(b). This noise floor is largely white with $1/f$ probe laser phase noise dominating at frequencies below approximately 100 kHz because of unequal interferometer path lengths in the homodyne detection, which results in uncanceled laser phase noise. The overall phase offset of each beat corresponds to the uncontrolled phase offset of the LO and signal frequency sources between each tone. The phase modulations of tones 1, 2, and 5 manifest as sinusoidal variations of the recovered phase, matching the phase deviation (90° peak-to-peak) and modulation rates applied. The

synthesizers for tones 3 and 4 are not modulated. The observed drifts in recovered phase instead correspond to the relative phase drift between the LO and signal channels for each synthesizer.

The total capacity for the Rydberg sensor to detect multiple tones is governed by the base-band instantaneous bandwidth, which is primarily set by the optical-spectroscopy method [16]. This measured bandwidth is shown in Fig. 3. Figures 3(a) and 3(b) are representative five-tone power spectra with different base-band detunings δ_i. In Fig. 3(a), all $\delta_i < 2\pi \times 1$ kHz and in Fig. 3(b), all δ_i are distributed over 20 MHz. The output reduction due to the instantaneous bandwidth roll-off is evident in Fig. 3(b). In Fig. 3(c), we directly measure the bandwidth by transmitting rf with a Fourier component of fixed amplitude and varying frequency. We accomplish this by varying the frequency of a phase modulation on tone $i = 2$. We fit the measured data to a double-pole low-pass filter [shown as the orange line in Fig. 3(c)] that has a 3-dB point of
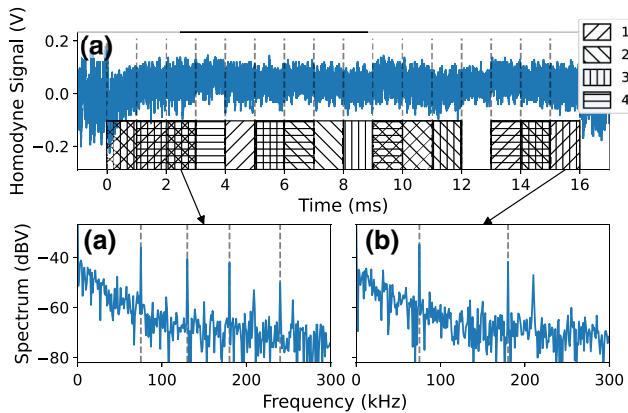
FIG. 4. Example symbol recovery of a communications signal. (a) The raw time trace of the EIT output from the photodetector, taken with a sample rate of 4 MS/s. The hashed boxes along the bottom axis denote which beat tones are on for each symbol period of 1 ms: tone 1 is the right diagonal, tone 2 is the left diagonal, tone 3 is the vertical, and tone 4 is the horizontal. (b) The FFT of the third symbol in the sequence. This symbol has all four tones on, their locations noted by gray-dashed vertical lines. (c) The FFT of the 15th symbol in the sequence. This symbol only has tones 1 and 3 on.

TABLE II. A bit-error summary of the OOK scheme under different signal amplitudes and symbol periods. The signal-field amplitudes are listed in order for $i = 1 - 4$. The bit rate (BR) is the corresponding data rate. The bit-error ratio (BE) shows the fraction of bits that are incorrectly received and the bit-error rate (BER) is the number of bit errors per unit time.

Signal fields (V/m)	Period (ms)	BR (kbit/s)	BE (%)	BER (kbit/s)
0.11, 0.13, 0.93, 2.0	1	4	0.2	7.8×10^{-3}
	0.1	40	1.5	6.1×10^{-1}
0.36, 0.41, 2.9, 6.3	1	4	0.05	1.9×10^{-3}
	0.1	40	0.01	2.8×10^{-3}

6.11(16) MHz. The number of individual beat tones that can be simultaneously measured depends on this bandwidth and the resolution bandwidth of the measurement. For example, using 10 kHz spacing between output beats as is done here, our 6.1 MHz bandwidth could nominally allow for 610 tones.

The application of many individual rf heterodyne pairs may be challenging due to the increased broadening of the Rydberg resonance with each LO and the potential for intermodulations between the beats, described above. It is possible to apply multiple signal beats to a single LO, helping to mitigate this limitation. In any case, the demonstration highlights the ability of the atoms to demodulate many highly disparate frequency tones (spanning 1.7–116 GHz) into a single base band, detected optically.

B. Communications

We perform four-band communication reception using an on-off-keying (OOK) protocol with tones 1–4 as described in the previous section, though far-off-resonant tones such as tone 5 could also be used. The OOK protocol does not encode information in the phase of the beats; however, the Rydberg sensor can observe the phase of each beat and the relative phase between beats. Protocols that encode information in these relative phases are interesting to consider but require transmitters to be phase synchronous. The four tones create 16 individual digital symbols, where an off tone represents a zero and an on tone represents a one. We step through these symbols, sending each for a fixed period of time, by turning the signal

sources on and off (the LOs stay on for the duration). An example is shown in Fig. 4, where each symbol is sent for 1 ms. Figure 4(a) is the raw time trace, with gray dashed vertical lines separating the time window of each symbol, and the hashed boxes denote which signal tones are on for each. We recover the symbol that is present by taking a Fourier transform in each window and comparing the amplitude at each beat frequency with a known fixed background level. Figures 4(b) and 4(c) show spectra for time windows 3 and 15. Window 3 has all tones on, while window 15 has only tones 1 and 3 on.

We measure the fidelity of symbol recovery under different experimental conditions by sending randomized symbol sequences and comparing the recovered OOK data stream with the known sent patterns. Table II displays the directly measured bit-error rates for the various settings, that include higher or lower signal fields (representing a difference of 10 dB in signal power) and symbol periods of 1 ms and 100 ms. For the slower symbol rate, representing a data rate of 4 kbit/s, the bit-error rate is better than 8×10^{-3} kbit/s. The faster symbol rate, yielding a data rate of 40 kbit/s, has bit-error rates better than 6.1×10^{-1} kbit/s.

This communication-reception demonstration is conceptually simple. However, it highlights the power of simultaneous data reception of multiple signal carriers spanning from 12 to 116 GHz. Given the broader capability of the Rydberg sensor, which includes full amplitude or phase demodulation of many tones (potentially > 100), it is possible to implement full quadrature-amplitude-modulated encoding for each signal tone, which would represent a complete orthogonal frequency-domain multiplexing protocol that can span multiple decades of the rf spectrum [17].

V. CONCLUSIONS

We show how to utilize the multiresonant response profile of a Rydberg atomic sensor to detect a wide range of rf tones. This intrinsic multiband nature of atoms is likely to lead to additional sensing capabilities in the future, where

it is difficult to achieve a similar ultrawide response profile using a sensor with a single resonant antenna. While the goal of this demonstration is not state-of-the-art sensitivity for Rydberg sensors, it shows a capability of such devices that cannot be easily mimicked by other physical platforms.

A primary remaining challenge is to improve the sensitivity of Rydberg sensors to weak fields. The fields detected in this work, for example, are of order 10^4 times stronger than those detected for Global Positioning System triangulation. However, this limitation is governed by constraints of the EIT-based spectroscopy method [18] and is not a limit inherent to atomic or quantum sensors. With further research, improved sensitivities are possible [2,19], yielding high-performance receivers that span a large section of the spectrum.

Another important avenue for study is to increase the instantaneous bandwidth of the Rydberg sensor. The current bandwidth roll-off near 6.1 MHz is governed by the EIT-based spectroscopy method. Alternative sensing schemes may improve this bandwidth, and therefore the multiplexing capacity, of Rydberg sensors used for ultrawideband detection.

APPENDIX A: RESONANT VERSUS OFF-RESONANT TWO-TONE RESPONSE

We show that off-resonant rf couplings to the target Rydberg state are generally necessary to satisfy the conditions of Eq. (1). We begin by defining an interaction Hamiltonian of our optically probed target Rydberg state coupled to two Rydberg states via rf fields with Rabi frequencies Ω_a, Ω_b and detunings δ_a, δ_b:

$$H = \frac{1}{2} \begin{pmatrix} 0 & \Omega_a & \Omega_b \\ \Omega_a & 2\delta_a & 0 \\ \Omega_b & 0 & 2\delta_b \end{pmatrix}. \qquad (A1)$$

We then determine the eigenfrequencies by diagonalizing this Hamiltonian. These eigenfrequencies represent the shifts of the coupled eigenstate energies from the bare Rydberg-target-state energy. It is these resonance shifts that are detected by performing EIT spectroscopy of the

Rydberg target state [see Fig. 1(a)(i)]. By analyzing the eigenfrequencies under different rf detunings, we can illustrate how multiple rf couplings to the same Rydberg state influence the observed spectroscopic shifts.

If both rf couplings are resonant with Rydberg transitions (δ_a, $\delta_b = 0$), the eigenfrequencies are the quadrature sum of both Rabi frequencies:

$$d\omega_{\text{res}} = \pm \frac{1}{2} \sqrt{\Omega_a^2 + \Omega_b^2}. \qquad (A2)$$

This quadrature sum prevents general linear mapping of the individual couplings into the sensor base band. While signal recovery is still possible with such a nonlinear response, the coupled shifts often lead to undesirable results. For example, if $\Omega_a \gg \Omega_b$, the shift for field b (and any corresponding beat signal) is reduced by an additional factor of $\Omega_b / 2\Omega_a$ and any beat in field b will not be independent of beats in field a.

If both rf couplings are off resonant with Rydberg transitions (δ_a, $\delta_b \neq 0$), the resulting eigenfrequencies show that the leading-order Stark shifts from each transition sum. If we impose the simplifying assumption that $\delta_i \gg \Omega_i$ and expand to lowest orders in Ω_i, the Stark shift of the target state is

$$d\omega_{\text{off-res}} = -\frac{\Omega_a^2}{4\delta_a} - \frac{\Omega_b^2}{4\delta_b} + \frac{\Omega_a^2\Omega_b^2}{16\delta_a\delta_b^2} + \frac{\Omega_a^2\Omega_b^2}{16\delta_a^2\delta_b}. \qquad (A3)$$

As expected, we observe that the total Stark shift of each coupling adds linearly into the sensor base band. By employing rf heterodyne detection for each tone, the signal response at each coupling is linearized, allowing for linear mapping of each signal tone into the sensor base band. Note that changing the signs of the detunings also allows for the cancelation of large dc shifts due to the LOs.

If one rf coupling is resonant and the other is detuned ($\delta_a \neq 0$, $\delta_b = 0$), one still observes linearly adding shifts from the two couplings. If we again impose that $\delta_a \gg \Omega_a$ and expand to lowest orders in Ω_a, we observe the new eigenfrequencies of the Hamiltonian to be

$$d\omega_{\text{mixed}} = \pm \frac{\Omega_b}{2} - \frac{\Omega_a^2}{8\delta_a}. \qquad (A4)$$

In essence, one observes a combination of Autler-Townes splitting and an ac Stark shift. Combined with the above derivations, this shows that Stark shifts can satisfy Eq. (1), as long as no more than one rf coupling is resonant. In future applications, this mode of operation could be used to increase the sensitivity of a single tone (by working on resonance), while maintaining wideband demodulation into the sensor base band for many off-resonant couplings.

APPENDIX B: EXPERIMENTAL DETAILS

The details of the experimental apparatus are described in Refs. [8,10]. Here, we summarize the most relevant aspects and any deviations from these works.

The homodyne probe field has a power of 3.6 μW and a $1/e^2$ radius of 410 μm. The corresponding Rabi frequency is $\Omega_p = 2\pi \times 3.1$ MHz. The probe-laser frequency is stabilized to a spectroscopy-referenced laser. When the probe laser is not being swept, its frequency is set to be single-photon resonant with the atomic transition for zero-velocity-class atoms ($\delta_p = 0$). The coupling laser has a power of 500 mW and a $1/e^2$ radius of 380 μm. The corresponding Rabi frequency, averaged over the $|m_J| = 1/2, 3/2$ couplings, is $\Omega_c = 2\pi \times 4.9$ MHz The coupling-laser frequency is stabilized to a ultra-low-expansion glass optical cavity. The coupling-laser frequency is set to be single-photon resonant with the atomic transition for zero-velocity-class atoms.

Balanced optical-homodyne detection is implemented using a Thorlabs PDB450A detector set to a gain of 10^5. The homodyne path phase is stabilized using an additional optical tone present on the probe laser, which is detected in heterodyne using a bias tee with both low- and high-pass port bandwidths of 32 MHz. The "dc" (homodyne) output of this bias tee is the source of all the data presented in this work.

We acquire data from the homodyne output in three primary ways: by USB-DAQ (see below), oscilloscope, and fast-Fourier-transform (FFT) spectrum analyzer. The first data-acquisition method is a sweep of the probe-beam frequency ω_p across its single-photon resonance, for a fixed ω_c. We then record the resulting EIT output [e.g., Fig. 1(c)] at 500 kS/s using a National Instruments USB 6343 data-acquisition system (USB-DAQ). The second method is to record time-domain voltage data using a Keysight DSOX3024T oscilloscope. From this, the data can be presented directly [Fig. 2(a)] or transformed to the frequency domain in postprocessing [Figs. 2(b)(i) and 2(b)(ii)] via FFT. The third method is to acquire power spectra directly using the FFT-spectrum-analyzer function of a multipurpose Liquid Instruments Moku:Lab (0–250 MHz input bandwidth). Where appropriate, we quote resolution bandwidths (RBWs) associated with measurements taken using this instrument.

We broadcast the five microwave tones (Table I) through free space onto the atomic sample. Each tone consists of a pair of frequencies, signal and LO, that are combined prior to emission from the same horn. The horns for tones 1–5 have gains of 20, 15, 25, 25, and 10 dBi, respectively. The frequencies for tones 1, 2, and 5 are generated by pairs of nearly identical frequency-synthesizer models; Rohde & Schwarz SM100B, Keysight 8257N/D, and Stanford Research Systems SG386, respectively. The signal chains generating tones 3 and 4 begin with seed

frequencies generated by two Windfreak SynthHD PRO synthesizers, each with two independent channels that we use for the signal and LO of the respective tone. We use Virginia Diodes rf multiplication modules to multiply the seed frequencies by a factor of 6 and provide amplification. The modules contain an internal voltage-controlled attenuator that we augment with manual waveguide attenuators on the output to provide fine power adjustments. The LAB-SCRIPT software suite is used for experimental hardware control and timing [20].

APPENDIX C: FIELD CALIBRATION

We calibrate rf field amplitudes at the atoms using the known spectroscopic response of the Rydberg target state. This response is calculated using the Floquet analysis developed in Ref. [10]. This model allows for arbitrary rf frequencies and properly accounts for Stark shifts from many Rydberg states simultaneously.

We first calibrate the LO-field amplitudes by measuring the amplitude of the Stark shift $d\omega_i$, with one LO field applied at a time, using a probe sweep measurement like those shown in Fig. 1(c). We then use the Floquet model to determine the field amplitude necessary to produce that shift, accounting for the reduction in observed shift due to Doppler effects in a probe sweep [16] and averaging the response between the nominally populated $|m_J| = 1/2, 3/2$ sublevels. The reported uncertainty in the field calibrations is due to statistical uncertainty in measuring $d\omega_i$ for each tone.

For tone 5, the carrier frequency is far enough from resonance that the response of the individual sublevels of the $56D_{5/2}$ state is more complicated than a simple global shift. To calibrate its field, we take a series of probe sweeps with the LO power varied around its set point and match the Floquet model to the observed shifts. The result is shown in Fig. 5, where the solid, dashed, and dotted lines represent the theory predictions of the Stark shifts for the $|m_J| = 1/2, 3/2$, and $5/2$ sublevels. Note that the contrast of the peak for the $|m_J| = 5/2$ transition is much lower than the other two sublevels. This indicates that this sublevel is not as strongly populated, which is to be expected due to the linear polarizations of all the optical fields, which preclude direct dipole-allowed coupling into that sublevel from the $5P_{3/2}$ intermediate state. These data and the corresponding model fit further indicate that the observed broadening shown in Fig. 1(c) is largely attributable to the sublevel structure of the Rydberg states that we are probing.

Calibration of the signal-field amplitudes is more difficult, as the weak field amplitudes do not give resolvable Stark shifts on their own. For tones 1, 2, and 5, the signal tone is generated by a signal source identical to the LO signal source and the two tones are combined using resistive power combiners with a power imbalance better than 0.2 dB. As such, we extrapolate the signal-field
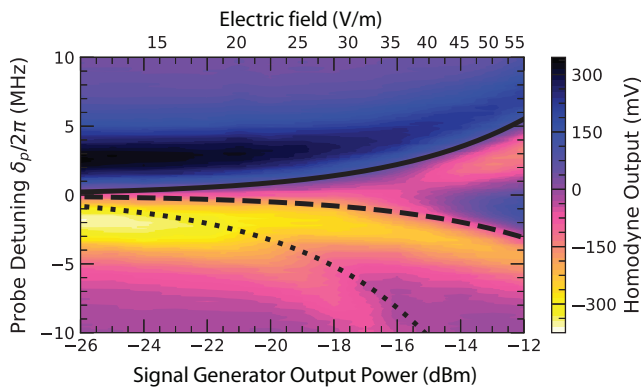
FIG. 5. An example calibration of the LO power for tone 5. Due to the large detuning from the nearest Rydberg transition, the atomic sublevels do not shift in the same direction. We match the Floquet-theory model to a range of LO rf powers as shown by the solid, dashed, and dotted lines, which track the zero crossing of the dispersive resonance for $|m_J| = 0.5, 1.5,$ and 2.5, respectively.

calibration from the LO-field calibration based on the difference in set points of the signal generators. For tones 3 and 4, this process is not reliable, as the multiplication modules are not guaranteed to amplify the LO and signal tones evenly. To calibrate these tones, we measure the beat amplitudes of tones 1 and 2 on a spectrum analyzer and use the derived LO and signal fields already calibrated to establish a conversion factor between the signal-field and the photodetector output voltage, employing Eq. (3). We then use this calibration factor to determine the signal-field amplitudes of tones 3 and 4 relative to the calibrated LO-field amplitudes.

APPENDIX D: DETECTOR BANDWIDTH CORRECTION

The bandwidth response of the sensor is limited, in part, by the photodetector bandwidth. We show an independently measured detector bandwidth curve in Fig. 6,
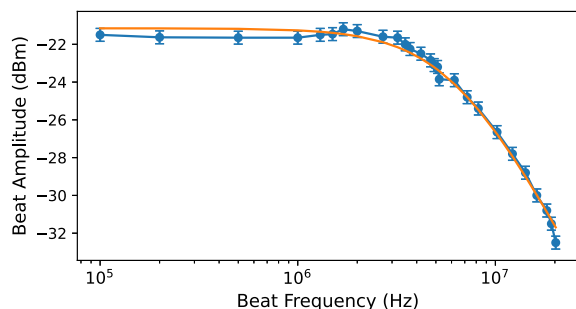

FIG. 6. The photodetector response as a function of the optical beat frequency. The error bars represent the measurement error and the orange line represents a single-pole roll-off fit with a corner at 6.30(14) MHz.

as well as a fit to a single-pole low-pass filter (orange line) with a 3-dB corner frequency at 6.30(14) MHz. It is obtained by tuning the applied EOM modulation frequency of the probe light, generating an optical beat of constant magnitude. We use the fitted low-pass-filter response to remove the detector contribution to the data of Figs. 3(b) and 3(c), revealing the intrinsic atomic response.

[1] J. A. Sedlacek, A. Schwettmann, H. Kübler, R. Löw, T. Pfau, and J. P. Shaffer, Microwave electrometry with Rydberg atoms in a vapour cell using bright atomic resonances, Nat. Phys. **8**, 819 (2012).

[2] C. S. Adams, J. D. Pritchard, and J. P. Shaffer, Rydberg atom quantum technologies, J. Phys. B: At., Mol. Opt. Phys. 53, 012002 (2019). ArXiv:1907.09231,

[3] C. L. Holloway, M. T. Simons, J. A. Gordon, A. Dienstfrey, D. A. Anderson, and G. Raithel, Electric field metrology for SI traceability: Systematic measurement uncertainties in electromagnetically induced transparency in atomic vapor, J. Appl. Phys. **121**, 233106 (2017).

[4] C. Holloway, M. Simons, A. H. Haddab, J. A. Gordon, D. A. Anderson, G. Raithel, and S. Voran, A multiple-band Rydberg atom-based receiver: AM/FM stereo reception, IEEE Antennas Propag. Mag. **63**, 63 (2021).

[5] M. T. Simons, A. B. Artusio-Glimpse, C. L. Holloway, E. Imhof, S. R. Jefferts, R. Wyllie, B. C. Sawyer, and T. G. Walker, Continuous radio-frequency electric-field detection through adjacent Rydberg resonance tuning, Phys. Rev. A 104, 032824 (2021). ArXiv:2105.10561,

[6] E. Paradis, G. Raithel, and D. A. Anderson, Atomic measurements of high-intensity VHF-band radio-frequency fields with a Rydberg vapor-cell detector, Phys. Rev. A **100**, 013420 (2019).

[7] Y.-Y. Jau and T. Carter, Vapor-Cell-Based Atomic Electrometry for Detection Frequencies below 1 kHz, Phys. Rev. Appl. 13, 054034 (2020). ArXiv:2002.04145,

[8] D. H. Meyer, P. D. Kunz, and K. C. Cox, Waveguide-Coupled Rydberg Spectrum Analyzer from 0 to 20 GHz, Phys. Rev. Appl. 15, 014053 (2021). ArXiv:2009.14383,

[9] D. A. Anderson, S. A. Miller, G. Raithel, J. A. Gordon, M. L. Butler, and C. L. Holloway, Optical Measurements of Strong Microwave Fields with Rydberg Atoms in a Vapor Cell, Phys. Rev. Appl. **5**, 034003 (2016).

[10] D. H. Meyer, Z. A. Castillo, K. C. Cox, and P. D. Kunz, Assessment of Rydberg atoms for wideband electric field sensing, J. Phys. B: At., Mol. Opt. Phys. **53**, 034001 (2020).

[11] L. A. Downes, A. R. MacKellar, D. J. Whiting, C. Bourgenot, C. S. Adams, and K. J. Weatherill, Full-Field Terahertz Imaging at Kilohertz Frame Rates Using Atomic Vapor, Phys. Rev. X 10, 011027 (2020). ArXiv:1903.01308,

[12] K. C. Cox, D. H. Meyer, F. K. Fatemi, and P. D. Kunz, Quantum-Limited Atomic Receiver in the Electrically Small Regime, Phys. Rev. Lett. **121**, 110502 (2018).

[13] M. T. Simons, A. H. Haddab, J. A. Gordon, and C. L. Holloway, A Rydberg atom-based mixer: Measuring the phase

of a radio frequency wave, Appl. Phys. Lett. **114**, 114101 (2019).

[14] M. Jing, Y. Hu, J. Ma, H. Zhang, L. Zhang, L. Xiao, and S. Jia, Atomic superheterodyne receiver based on microwave-dressed Rydberg spectroscopy, Nat. Phys. 16, 911 (2020). ArXiv:1902.11063,

[15] This and other frequency definitions in this work are defined in units of rad/s. However, we often specify them in hertz; so a beat frequency of 100 Hz would be interpreted as $\delta = 2\pi \times 100$ Hz.

[16] D. H. Meyer, K. C. Cox, F. K. Fatemi, and P. D. Kunz, Digital communication with Rydberg atoms and amplitude-modulated microwave fields, Appl. Phys. Lett. **112**, 211108 (2018).

[17] L. S. Hanzo and W. Webb, *Single- and Multi-Carrier Quadrature Amplitude Modulation* (John Wiley & Sons, Ltd., 2000).

[18] D. H. Meyer, C. O'Brien, D. P. Fahey, K. C. Cox, and P. D. Kunz, Optimal atomic quantum sensing using electromagnetically-induced-transparency readout, Phys. Rev. A **104**, 043103 (2021).

[19] H. Fan, S. Kumar, J. Sedlacek, H. Kübler, S. Karimkashi, and J. P. Shaffer, Atom based RF electric field sensing, J. Phys. B: At., Mol. Opt. Phys. **48**, 202001 (2015).

[20] P. T. Starkey, C. J. Billington, S. P. Johnstone, M. Jasperse, K. Helmerson, L. D. Turner, and R. P. Anderson, A scripted control system for autonomous hardware-timed experiments, Rev. Sci. Instrum. **84**, 085111 (2013).